Filtering and functional parameter estimation of spatiotemporal strong-dependence models

María Pilar Frías
Department of Statistics
and Operations Research,
University of Jaén, Spain

María Dolores Ruiz-Medina
Department of Statistics
and Operations Research,
University of Granada, Spain

Abstract

Filtering and parameter estimation are addressed in the context of spatiotemporal strong dependence processes. A functional parametric observation model is fitted to the spectral sample information. Specifically, the class of strong dependence spatiotemporal random fields studied in Frías, Ruiz-Medina, Alonso, and Angulo (2006a), Frías, Ruiz-Medina, Alonso, and Angulo (2008), Frías, Ruiz-Medina, Alonso, and Angulo (2009) is considered. Large dimensional spectral data sets, displaying high local singularity, are then processed in this functional setting. Thresholding techniques are first applied for removing noise generated from measurement spectrometer device. Spatiotemporal long-range dependence model fitting is then achieved by applying linear regression in the log-wavelet domain. The performance of the estimation algorithms proposed is illustrated from simulated data.

Keywords: Fractal spectral processes, long-range dependence parameters, spatiotemporal parametric models, wavelet thresholded transform.

1. Introduction

Remote Sensing of Environment constitutes a crucial task in assessment of urban heat island effect, surface soil water content, green vegetation, climate change, etc. (see Byambakhuu, Sugita, and Matsushima (2010); Elvidge, Chen, and Groeneveld (1993); Gallo, McNab, Karl, Brown, Hood, and Tarpley (1993); Price (1990), among others). Imaging spectrometry is one of the most common tools used for capturing sample information from the earth (see, for example, Bell, B.A., and Martini (2010); Clark and Roush (1984); Goetz, Vane, Solomon, and Rock (1985)). This paper contributes to the analysis of spatiotemporal data in this context,

since functional data are collected in the spectral domain, focusing our study to the case of strong correlations in space and time. That is, the collected functional spectral data displays a singularity at the origin (see, Leonenko (1999) and Frías *et al.* (2009)), considering the statistical functional framework (see, Delicado, Giraldo, Comas, and Mateu (2009)).

In the spatial statistical analysis of high dimensional data sets, for example, in the investigation of soil properties, air ozone concentration, velocity turbulence fields, ocean surface temperature profiles from deep ocean weather stations, often strong correlations are detected in time and or space (see, for example, Akkaya and Yücemen (2002), Anh, Lam, Leung, and Tieng (2000), Marguerit, Schertzed, Schmitt, and Lovenjoy (1998)). For the analysis of high-dimensional data usually dimension reduction techniques are applied. In the strong-dependence case these techniques must be combined with the truncation of the heavy tails of the underlying covariance model. In particular, this fact corresponds to the truncation of the singularity at zero of the associated spectral density, which provides information on the behavior of the covariance function at large lags. The hyperbolic rate displayed by the decay velocity of the covariance function of strong-correlated random fields induces serious difficulties in the implementation of inference tools (see, Frías *et al.* (2009)). This fact hinders the development of functional estimation algorithms, since several model selection and matrix computational problems arise. Some attempts have been made in the parametric and semi-parametric spatial and spatiotemporal estimation contexts (see Bardet, Lang, Oppenheim, Philippe, Stove, and Taqqu (2003), Frías *et al.* (2006a), Frías *et al.* (2008), Frías *et al.* (2009), among others). A complete overview on statistical inference tools for random fields with singular spectra can be found in Leonenko (1999) (see also Kelbert, Leonenko, and Ruiz-Medina (2005)).

The measurement noise associated with devices, like spectrometers, increases the high local singular nature of spectral data, whose covariance function is heavy-tailed. This fact motivates the methodology proposed in this paper for addressing the problem of spatiotemporal long-range dependence model fitting from noisily large-dimensional spectral data. Specifically, the wavelet domain is first considered to transform the large-dimensional spectral data into functional data. Thresholding techniques are applied to the empirical wavelet coefficients for removing the observation noise (see, for example, Donoho and Johnstone (1995)). Linear regression estimates are then computed from the log-thresholded wavelet transform to approximate the temporal and spatial long-range dependence parameters.

The estimation approach presented in this paper can also be applied to the functional non-parametric regression context in the case where the functional regressors display strong correlation (see Ferraty, Goia, and Vieu (2002), under the weak-dependence modeling, and Benhenni, Hedli-Griche, Rachdia, and Vieu (2008), under long memory conditions). In the Geostatistical framework, spatiotemporal kriging and functional parameter estimation, under strong dependence modeling, can also be addressed from the application of the estimation methodology formulated here. In this context, we mention the papers by Delicado *et al.* (2009), Baladandayuthapani, Mallick, Hong, Lupton, Turner, and Caroll (2008) and Basse, Diop, and Dabo-Niang (2008) on statistical analysis of functional data displaying spatial interaction (see also Ruiz-Medina (2011), in the spatial autoregressive functional context).

The outline of the paper is the following. The spatiotemporal strong dependence functional model, assumed in the development of the results presented in this paper, is introduced in Section 2. The filtering and parameter estimation methodology proposed are described in Section 3. A simulation study is carried out in Section 4 for illustration of the wavelet-based

filtering and long-range dependence model fitting approach presented in the spectral domain. A real-data example is considered in Section 5 to illustrate the methodology proposed. Concluding remarks are given in Section 6.

2. Statistical functional model

Let us consider the following functional spectral observation model:

$$Z(\omega, \boldsymbol{\lambda}) = \widehat{X}(\omega, \boldsymbol{\lambda}) + \varepsilon(\omega, \boldsymbol{\lambda}), \quad (\omega, \boldsymbol{\lambda}) \in \mathbb{R}^{d+1}.$$

Here, ε denotes functional spectral Gaussian observation noise, that is, $\varepsilon \in H$, $E[\varepsilon] \equiv 0$, and

$$E[\varepsilon \otimes \varepsilon] = \sigma_\varepsilon^2 \mathbf{I},$$

where $\mathbf{I}$ is the identity operator on $\mathbb{R}^{d+1}$. Process ε is also assumed to be uncorrelated with $\widehat{X}$. By H we denote a separable Hilbert space of spatiotemporal functions, assumed to be included in $L^2(\mathbb{R}^{d+1})$, the space of square integrable function on $\mathbb{R}^{d+1}$. The spectral functional random variable $\widehat{X} \in H$ is defined from the realizations of the spectral process associated with a Gaussian long-range dependence spatiotemporal random field X given by:

$$X(t, \mathbf{z}) \underset{m.s}{=} \int_{\mathbb{R}^{d+1}} r(t - s, \mathbf{z} - \mathbf{y}) Y(s, \mathbf{y}) ds d\mathbf{y}, \tag{1}$$

where

$$r(t, \mathbf{z}) = |t|^{-1+\nu} \prod_{i=1}^{d} |z_i|^{-1+\beta_i}, \tag{2}$$

with $(\nu, \beta_1, \dots, \beta_d) \in (0, 1/2)^{d+1}$, $t \in \mathbb{R}$, $\mathbf{z} \in \mathbb{R}^d$. Note that, kernel r displays an anisotropic heavy-tail behavior, inducing a local multi-self-similar behavior of our functional spectral data in a neighborhood of zero-frequency. The input spatiotemporal random field Y of model (1) satisfies the following conditions, needed for the pointwise definition of X (see Leonenko (1999), Adler (1981) and Ruiz-Medina, Ángulo, and Anh (2003)):

Condition 1.
$$|f_Y(\omega, \boldsymbol{\lambda})| \longrightarrow C_1,$$

when $\omega \longrightarrow 0$ and $\boldsymbol{\lambda} = (\lambda_1, \dots, \lambda_d)$, $\lambda_i \longrightarrow 0$, for $i = 1, \dots, d$, with C_1 being a positive constant and f_Y the spectral density of the spatiotemporal process Y.

Condition 2.
$$\frac{|f_Y(\omega, \boldsymbol{\lambda})|}{(1 + |(\omega, \boldsymbol{\lambda})|^2)^{-\widetilde{\nu} - \sum_{i=1}^{d} \widetilde{\beta}_i}} \longrightarrow C_2,$$

when $\omega \longrightarrow \infty$ and $\lambda_i \longrightarrow \infty$, for $i = 1, \dots, d$, and for $\boldsymbol{\lambda} = (\lambda_1, \dots, \lambda_d)$, where C_2 is a positive constant, $(\widetilde{\nu}, \widetilde{\beta}_1, \dots, \widetilde{\beta}_d) \in (1/2, 1)^{d+1}$, and f_Y denotes, as before, the spectral density of the *input* spatiotemporal process Y.

Remark 1 *Note that Condition 1 means that the integrability order of the spectral density of the spatiotemporal process X at zero frequency depends only of the behavior of the Fourier transform $\hat{r}(\omega, \boldsymbol{\lambda}) = |\omega|^{-\nu} \prod_{i=1}^{d} |\lambda_i|^{-\beta_i}$ of kernel r, at a neighborhood of zero-frequency. This*

behavior is characterized in terms of the range of the parameter vector $(\nu, \beta_1, \ldots, \beta_d)$ (which determines the integrability of the spectral density f_X at the origin). Specifically, the integrability at zero of f_X holds for $(\nu, \beta_1, \ldots, \beta_d) \in (0, 1/2)^{d+1}$. On the other hand, the asymptotic order at infinity of the spectral density f_X of X depends on the considered ranges for vectors $(\nu, \beta_1, \ldots, \beta_d)$ and $(\widetilde{\nu}, \widetilde{\beta}_1, \ldots, \widetilde{\beta}_d)$. In this case, for $\widetilde{\nu} > (1/2) - \nu$ and $\widetilde{\beta}_i > (1/2) - \beta_i$, for $i = 1, \ldots, d$, f_X is absolutely integrable at infinity.

3. Estimation methodology

As commented, from Condition 1, the spectral density f_X of spatiotemporal process X displays the following asymptotic local fractal behavior, when $|\omega| \to 0$, and $|\lambda_i| \to 0$, $i = 1, \ldots, d$, (see, Leonenko (1999)),

$$f_X(\omega, \boldsymbol{\lambda}) \sim C_1 |\omega|^{-2\nu} \Pi_{i=1}^d |\lambda_i|^{-2\beta_i}, \ \nu \in (0, 1/2), \ \beta_i \in (0, 1/2), \ i = 1, \ldots, d. \tag{3}$$

In the implementation of the functional estimation algorithms formulated below, compactly supported orthonormal wavelet bases are considered. The multiresolution analysis of $L^2(\mathbb{R}^{d+1})$ is performed in terms of the tensorial product of $d + 1$ one-dimensional orthonormal wavelet bases (see, Meyer (1992)). The one-dimensional wavelet transforms are defined in terms of a scaling basis $\{\phi_k : k \in \Gamma_0 \subset \mathbb{Z}\}$ of a coarsest scale space V_0, and a sequence of wavelet bases $\{\psi_{j:k} : k \in \Lambda_j \subset \mathbb{Z}, \ j \geq 0\}$ of the detail space sequence $\{W_j, \ j \geq 0\}$. The index sets Γ_0 and Λ_j, for $j \geq 0$, are constituted by the integer values k defining the needed translations for covering, at different resolution levels, the one-dimensional zero-frequency neighborhoods considered at the temporal, and at each one of the main spatial directions, in the estimation algorithms described below. Suitable examples of such bases can be constructed from the tensorial product of Haar and Daubechies systems.

To remove the local variability represented by parameter σ_ε^2, due to the measurement noise, universal wavelet thresholding is applied to the empirical wavelet spectral coefficients. That is, we consider the universal threshold UT defined by

$$UT = \sigma_\varepsilon \sqrt{2 \log n},$$

where n denotes the sample size. Here, we have chosen UT, since the noise ε, resulting from the spectral instrument error, is assumed to be Gaussian distributed (see Donoho and Johnstone (1995)). Alternative thresholding rules must be considered for going beyond the Gaussian assumption in order to preserve signal energy, e.g. Lorenz Thresholding (see Vidakovic (1999)).

Under Conditions 1 and 2, the following asymptotic identities are obtained for the wavelet transform of the square-root, $f_X^{1/2}$, of the spectral density f_X, when $R \to 0$,

$$f_{j:k}^1 = \int_{[-R,R]} f_Y^{1/2}(\omega, \boldsymbol{\lambda^0}) |\omega|^{-\nu} \prod_{i=1}^d |\lambda_i^0|^{-\beta_i} \psi_{j:k}(\omega) d\omega \sim 2^{-j(-\nu+1/2)} C(\psi, \boldsymbol{\lambda^0}), \tag{4}$$

for a fixed spatial frequency value $\boldsymbol{\lambda^0}$ in a neighborhood of the spatial zero frequency, where $[-R, R]$ denotes a one-dimensional interval of length $2R$ containing the point zero, and

$C(\psi, \boldsymbol{\lambda^0})$ is a constant depending on the wavelet basis chosen and on the fixed spatial frequency value $\boldsymbol{\lambda^0}$. Specifically, under condition 1,

$$C(\psi, \boldsymbol{\lambda^0}) \sim C_1 \prod_{i=1}^{d} |\lambda_i^0| \int_{[-R,R]} |s|^{-\nu} \psi(s-k) ds.$$

Here, for $k \in \Lambda_j$ and $j \geq 0$, $f_{j:k}^1$ denotes the one-dimensional temporal wavelet coefficient of the square-root $f_X^{1/2}$ of the spectral density f_X of our random field of interest X, evaluated at $\boldsymbol{\lambda^0}$, with respect to the element $\psi_{j:k}$ of the wavelet basis selected. Similarly, when $R \to 0$, we have

$$
\begin{aligned}
f_{j:k}^{1+i} &= \int_{[-R,R]} f_Y^{1/2}(\omega^0, \lambda_1^0, \ldots, \lambda_i, \ldots, \lambda_d^0) \\
&\qquad \times |\omega^0|^{-\nu} |\lambda_1^0|^{-\beta_1} \cdots |\lambda_i|^{-\beta_i} \cdots |\lambda_d^0|^{-\beta_d} \psi_{j:k}(\lambda_i) d\lambda_i \\
&\sim 2^{-j(-\beta_i+1/2)} C(\psi, \omega^0, \ldots, \lambda_{i-1}^0, \lambda_{i+1}^0, \ldots, \lambda_d^0), \quad i = 1, \ldots, d,
\end{aligned}
\tag{5}
$$

where, as before, $C(\psi, \omega^0, \lambda_1 \ldots, \lambda_{i-1}^0, \lambda_{i+1}^0, \ldots, \lambda_d^0)$ is a constant depending on the wavelet basis chosen, and on the fixed frequency values $\omega^0, \ldots, \lambda_{i-1}^0, \lambda_{i+1}^0, \ldots, \lambda_d^0$ in a neighborhood of zero frequency. For instance, under Condition 1,

$$
\begin{aligned}
C(\psi, \omega^0, \ldots, \lambda_{i-1}^0, \lambda_{i+1}^0, \ldots, \lambda_d^0) &\sim C_1 |\omega^0|^{-\nu} |\lambda_1^0|^{-\beta_1} \cdots |\lambda_{i-1}^0|^{-\beta_{i-1}} |\lambda_{i+1}^0|^{-\beta_{i+1}} \cdots |\lambda_d^0|^{-\beta_d} \\
&\qquad \times \int_{[-R,R]} |s|^{-\beta_i} \psi(s-k) ds.
\end{aligned}
$$

Here, for $k \in \Lambda_j$, $j \geq 0$, and $i = 1, \ldots, d$, $f_{j:k}^{1+i}$ denotes, as in the temporal case, the one-dimensional spatial wavelet coefficient of the square-root

$$
\begin{aligned}
f_X^{1/2}(\omega^0, \ldots, \lambda_{i-1}^0, \cdot, \lambda_{i+1}^0, \ldots, \lambda_d^0) &= f_Y^{1/2}(\omega^0, \ldots, \lambda_{i-1}^0, \cdot, \lambda_{i+1}^0, \ldots, \lambda_d^0) \\
&\qquad \times |\omega^0|^{-\nu} \prod_{j=1, j \neq i}^{d} |\lambda_j^0|^{-\beta_j} |\cdot|^{-\beta_i}
\end{aligned}
\tag{6}
$$

of the spectral density f_X of our random field of interest X, with respect to the element $\psi_{j:k}$ of the wavelet basis selected. Note that, under Conditions 1 and 2, f_Y admits a spectral factorization, that is, there exists $f_Y^{1/2}$ satisfying $f_Y = f_Y^{1/2} \overline{f_Y^{1/2}}$, with $\overline{f_Y^{1/2}}$ denoting the complex conjugate. This fact allows the definition, as in equation (6), of the square-root $f_X^{1/2}$ of the spectral density of process X, in terms of the square-root $f_Y^{1/2}$ of f_Y, as well as in terms of the Fourier transform $\widehat{r}$ of kernel r. Thus, equations (4)-(5) can be explicitly computed, and the temporal memory parameter ν and spatial dependence parameters β_i, $i = 1, \ldots, d$, can be estimated from the following equations:

$$\log_2 f_{j:k}^1 = -j(-\nu + 1/2) + \log_2 C(\psi, \boldsymbol{\lambda^0}), \tag{7}$$

$$\log_2 f_{j:k}^{1+i} = -j(-\beta_i + 1/2) + \log_2 C(\psi, \omega^0, \ldots, \lambda_{i-1}^0, \lambda_{i+1}^0, \ldots, \lambda_d^0), \tag{8}$$

for $i = 1, \ldots, d$.

The following functional filtering and parameter estimation algorithms are proposed.

Algorithm 1:

Step 1: Define the zero frequency neighborhood sequences: In time

$$[-R_j, R_j] \times [-\boldsymbol{\lambda}^{0,l}, \boldsymbol{\lambda}^{0,l}]^d, \quad j \in \mathbb{N},$$

for each $l = 1, \ldots, L_0$, and $\{\boldsymbol{\lambda}^{0,l}\}_{l=1}^{L_0}$ being a set of fixed spatial frequency vectors with decreasing positive real components, and $R_j \to 0$, as $j \to \infty$. Define also, in the space, for each $i = 1, \ldots, d$, the sequence

$$[-\omega^{0,l}, \omega^{0,l}] \times \cdots \times [-\lambda_{i-1}^{0,l}, \lambda_{i-1}^{0,l}] \times [-R_j, R_j] \times [-\lambda_{i+1}^{0,l}, \lambda_{i+1}^{0,l}] \times, \cdots \times [-\lambda_d^{0,l}, \lambda_d^{0,l}],$$

for $j \in \mathbb{N}$, and with $\{\omega^{0,l}\}_{l=1}^{L_0}$ $\{\lambda_m^{0,l}\}_{l=1}^{L_0}$, for $m = 1, \ldots, d$, $m \neq i$, being decreasing positive numbers sets in the spatial frequency domain, and, as before, $R_j \to 0$, as $j \to \infty$. These sequences of frequency sets provide the supports where the spectral process $\hat{X}$ is evaluated.

Step 2: For each $n \in \mathbb{N}$, compute the average on $l = 1, \ldots, L_0$, of the temporal sample spectral curves, which represent the evaluation of process $\hat{X}$ for $\omega \in [-R_j, R_j]$, for a fixed $\boldsymbol{\xi}^{0,l} \in [-\boldsymbol{\lambda}^{0,l}, \boldsymbol{\lambda}^{0,l}]^d$, and the average of the spatial sample spectral curves, which represent the evaluation of process $\hat{X}$ for $\lambda_i \in [-R_j, R_j]$, for each $i = 1, \ldots, d$, and considering fixed $\tau^{0,l} \in [-\omega^{0,l}, \omega^{0,l}]$, $\xi_m^{0,l} \in [-\lambda_m^{0,l}, \lambda_m^{0,l}]$, $m = 1, \ldots, d$, $m \neq i$, and $l = 1, \ldots, L_0$.

Step 3: Apply the one-dimensional wavelet transform to each element of the averaged temporal and spatial spectral curve sequence obtained in Step 2.

Step 4: Universal wavelet threshold is considered for removing noise in the wavelet coefficients computed in Step 3.

Step 5: At each zero frequency neighborhood, derive from equations (7) and (8), applying linear regression, estimates $\hat{\nu}$ and $\hat{\beta}_i$, $i = 1, \ldots, d$, of the temporal and spatial long-range dependence parameters.

Step 6: The arithmetic mean of the $d+1$ parameter estimate sequences derived in the previous step is computed.

Algorithm 2:

Step 1: It is given as in Algorithm 1.

Step 2: For each $j \in \mathbb{N}$, and for each $l = 1, \ldots, L_0$, compute the wavelet transform of the temporal sample spectral curves which represent the evaluation of process $\hat{X}$ for $\omega \in [-R_j, R_j]$, and for fixed $\boldsymbol{\xi}^{0,l} \in [-\boldsymbol{\lambda}^{0,l}, \boldsymbol{\lambda}^{0,l}]^d$, and of the spatial sample spectral curves, which represent the evaluation of process $\hat{X}$ for $\lambda_i \in [-R_j, R_j]$, for each $i = 1, \ldots, d$, and for fixed $\tau^{0,l} \in [-\omega^{0,l}, \omega^{0,l}]$, and $\xi_m^{0,l} \in [-\lambda_m^{0,l}, \lambda_m^{0,l}]$, $m = 1, \ldots, d$, $m \neq i$, and $l = 1, \ldots, L_0$.

Step 3: It coincides with Step 4 of Algorithm 1.

Step 4: It coincides with Step 5 of Algorithm 1.

Step 5: At each element of the zero frequency neighborhood sequences, average the temporal and spatial long-range dependence parameter estimates obtained in Step 4.

Step 6: It is defined as in Algorithm 1.

A third estimation algorithm, Algorithm 3, is defined considering in Algorithm 2 a smoothing version of the wavelet transform, with respect to the translation parameter at each resolution level. Finally, the formulation of Algorithm 1 in terms of a smoothing version, over the translation parameter, of the wavelet transform leads to Algorithm 4. As commented, in all the cases, universal wavelet threshold is considered, for removing the observation noise from the functional spectral data (see, for example, Vidakovic (1999)).

4. Simulations

A simulation study is developed to show the performance of the functional estimation algorithms proposed. Two spatiotemporal Gaussian stationary models, defining processes X_1 and X_2, are considered, having the following spectral densities:

$$
\begin{aligned}
f_{X_1}(\omega, \lambda_1, \lambda_2) &= \left[\frac{1}{(1+|\omega|^2)^{\alpha_1}}\right]\left[\frac{1}{(1+|\lambda_1|^2)^{\alpha_2}}\right]\left[\frac{1}{(1+|\lambda_2|^2)^{\alpha_3}}\right] \\
&\times \ |\omega|^{-2\nu}|\lambda_1|^{-2\beta_1}|\lambda_2|^{-2\beta_2},
\end{aligned}
\tag{9}
$$

with $\alpha_i \in (1/2, \infty)$, $i = 1, 2, 3$, and

$$
\begin{aligned}
f_{X_2}(\omega, \lambda_1, \lambda_2) &= \left[\frac{1}{1+|\omega|^{2\alpha_1}}\right]\left[\frac{1}{1+|\lambda_1|^{2\alpha_2}}\right]\left[\frac{1}{1+|\lambda_2|^{2\alpha_3}}\right] \\
&\times \ |\omega|^{-2\nu}|\lambda_1|^{-2\beta_1}|\lambda_2|^{-2\beta_2},
\end{aligned}
\tag{10}
$$

with $\alpha_i \in (1/2, \infty)$, $i = 1, 2, 3$, respectively. Note that, for $\alpha_i \in (1/2, 3/2)$, the above Gaussian models also display anisotropic fractality. Functional spectral data are constructed from $256 \times 256 \times 256$ frequency points belonging to the interval $[-127.5 * 10^{-8}, 127.5 * 10^{-8}]$, that is, $(\omega, \lambda_1, \lambda_2) \in [-127.5 * 10^{-8}, 127.5 * 10^{-8}]^3$, with discretization step size 10^{-8}. The simulation study is developed considering two structural parameter scenarios, corresponding to heavy and slight spectral singularity, in the range of strong dependence for the two-above introduced spectral models. In relation to the observation noise, we consider the parameter values $\sigma_\varepsilon = 2 * 10^2$ and $\sigma_\varepsilon = 0.05 * 10^2$, which keep a reasonable signal to noise ratio, according to the truncated spectral density values at a zero-frequency spectral neighborhood. That is, we consider the cases:

Case I: $\nu = 0.375$, $\beta_1 = 0.385$, $\beta_2 = 0.395$, $\alpha_1 = 0.7$, $\alpha_2 = 0.8$, $\alpha_3 = 0.9$,
Case II: $\nu = 0.185$, $\beta_1 = 0.195$, $\beta_2 = 0.205$, $\alpha_1 = 0.7$, $\alpha_2 = 0.8$, $\alpha_3 = 0.9$.

From equations (7) and (8) the following estimates can be derived by performing linear regression in the spectral log-wavelet domain:

$$
\hat{\nu} = -\hat{\theta}^{d+1} + \frac{1}{2}, \qquad \hat{\beta}_i = -\hat{\theta}^i + \frac{1}{2}, \quad i = 1, \ldots, d,
$$

where for $i = 1, \ldots, d+1$, $\hat{\theta}^i$ is computed by applying linear regression. Functional estimation algorithms 1, 2, 3 and 4 are implemented from the following spectral curve sample sizes

$n = 16, 36, 100, 400, 900, 1600, 2500, 3600, 4900, 6400$, at temporal and spatial directions. Figures 1-10 display the long-range dependence parameter estimate sequences, and the estimation of their standard deviation after applying Algorithms 1-4, as well as alternative estimation methods, the partially-integrated method and the marginal-integrated method, previously proposed in Frías, Ruiz-Medina, Alonso, and Angulo (2006) and Frías *et al.* (2009), respectively. Specifically, Case I in model (9), with $\sigma_{\varepsilon_2} = 2 * 10^2$, is displayed in Figures 1 and 2, where $\hat{\nu}$ (red), $\hat{\beta}_1$ (green) and $\hat{\beta}_2$ (blue) values are showed at the top, and standard deviations at the bottom. Dotted line represents the true parameter values. Continuous line provides the results on estimate value sequences after applying hard threholding, i.e., after filtering the spectral data. Dashed line represents the parameter estimate values without previous thresholding.

Figures 3 and 4 show the results obtained for case II and model (9), with $\sigma_{\varepsilon_2} = 2 * 10^2$. The same colors and lines are established for representing estimate value sequences and standard deviations without and with hard thresholding, as well as true parameter values. Figures 5-8 provide the estimation results for: Case I and model (10), with $\sigma_{\varepsilon_2} = 2 * 10^2$; Case II and model (10), with $\sigma_{\varepsilon_2} = 2*10^2$. Finally, 9-10 show Case I and model (10) with $\sigma_{\varepsilon_2} = 0.05*10^2$, and Case II and model (9) with $\sigma_{\varepsilon_2} = 0.05 * 10^2$.

The results displayed show a better performance of Algorithms 1 and 2 than Algorithms 3 and 4 for high local order of singularity of the spectral density. Additionally, thresholding improves the parameter estimation results in most of the cases considered with Algorithms 1 and 2. Note that, Algorithm 3 and 4 are not compatible with hard-thresholding. They provide better results when the lowest levels of structural and noise local variability are considered. Thus, Algorithms 1 and 2 outperform Algorithms 3 and 4 in the higher local singular cases, and the discrimination between signal and noisy energies, achieved by applying thresholding, improves the parameter estimation results, for a suitable signal to noise ratio. In comparison with the previous estimation methodologies implemented in Frías *et al.* (2006) and Frías *et al.* (2009), the partially-integrated method and the marginal-integrated method, a better performance is obtained with Algorithms 1 and 2, when Case I is considered, in relation to the accuracy of the estimations. It should be noted that estimators with Algorithms 1 and 2 display similar empirical variability properties to those ones presented by previously designed methods in Frías *et al.* (2006) and Frías *et al.* (2009).

5. Application

In this section, the performance of the estimation algorithms proposed is illustrated with a real-data example. The data set studied consists of mean annual daily ocean surface temperature profiles with data size equal to 250 observations, collected from weather stations in the Hawaii Ocean and the West Coast of the United States (latitude-longitude interval $[21.34, 49.98] \times [-158.361, -120, 90]$). In particular, the year 2000 is analyzed at 256 weather stations, according to the availability of the public oceanographic bio-optical database, *The Worldwide Ocean Optics Database (WOOD)*, from which data are collected. The fast Fourier transform is applied to mean annual daily temperature profiles to implement Steps 1-6 of Algorithms 1-4, in terms of the corresponding temporal and spatial spectral curves. Haar wavelet transform is applied in all the cases. Figure 11 shows the long-range dependence parameter estimate sequences, and the estimation of their standard deviations after applying Algorithms 1-4. The spectral curve sample sizes used at temporal and spatial directions are
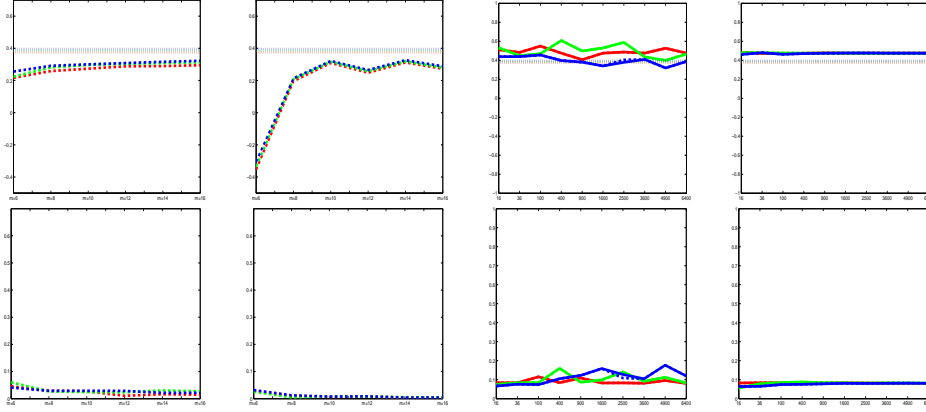
Figure 1: $\hat{\nu}$, $\hat{\beta}_1$, and $\hat{\beta}_2$ values (top) and standard deviations (bottom), partially-integrated method (left), marginal-integrated method (left-medium), algorithm 1 (right-medium), algorithm 2 (right), for case I and for model (9) with $\sigma_{\varepsilon_2} = 2*10^2$. The values on horizontal axis represent the spectral curve sample sizes considered.

$\hat{\sigma}(\hat{\nu})$	Algorithm 1	Algorithm 2	Algorithm 3	Algorithm 4
$n = 4$	0.0134	0.0155	0.3253	0.3195
$n = 9$	0.0113	0.0120	0.3406	0.3313
$n = 16$	0.0109	0.0113	0.2951	0.5369
$n = 25$	0.0119	0.0122	0.2876	0.2847
$n = 36$	0.0125	0.0126	0.2556	0.2551
$n = 49$	0.0123	0.0125	0.2431	0.2462
$n = 64$	0.0110	0.0111	0.2127	0.2198
$n = 81$	0.0200	0.0201	0.2014	0.2304
$n = 100$	0.0182	0.0182	0.1886	0.2125
$n = 121$	0.0167	0.0168	0.1783	0.1986

Table 1: Standard deviation of $\hat{\nu}$ values.

$n = 4, 9, 16, 25, 36, 49, 64, 81, 100, 121$. Standard deviations of $\hat{\nu}$, $\hat{\beta}_1$ and $\hat{\beta}_2$ are also displayed in Tables 1-3. As showed in the simulation study, Algorithms 1 and 2 are more efficient than Algorithms 3 and 4. Note that the spatial strong dependence is induced by the high concentration level of weather stations. Since this concentration is similar in terms of longitude and latitude magnitudes, the two spatial long-range dependence parameters are very close. This fact is reflected in the results displayed in Figure 11.
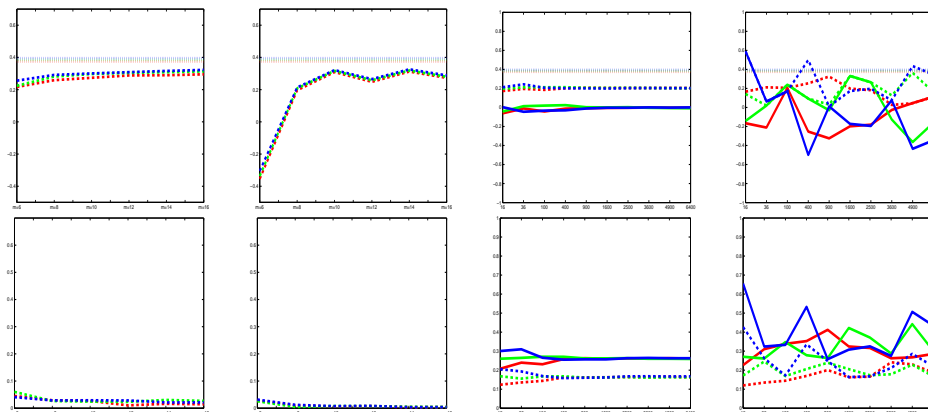
For comparative purposes, considering the same functional data sets, the previous spectral-based estimation methodologies proposed in Frías *et al.* (2006) and Frías *et al.* (2009) are also applied for estimation of the temporal and spatial long-range dependence parameters in the spectral domain (see Figure 12). As in the simulation study, it can be appreciated that similar empirical variability properties are displayed by the estimates computed with the previous spectral methods in Frías *et al.* (2006) and Frías *et al.* (2009), and with Algorithms 1 and 2 in the spectral- wavelet domain. However, although similar estimates are obtained, with both methodologies, for the spatial long-range dependence parameters, bigger differences are

$\hat{\sigma}(\hat{\beta}_1)$	Algorithm 1	Algorithm 2	Algorithm 3	Algorithm 4
$n = 4$	0.0399	0.0299	0.0020	0.0019
$n = 9$	0.0359	0.0265	0.0033	0.0032
$n = 16$	0.0326	0.0226	0.0029	0.0029
$n = 25$	0.0268	0.0198	0.0032	0.0032
$n = 36$	0.0224	0.0174	0.0068	0.0067
$n = 49$	0.0207	0.0165	0.0095	0.0094
$n = 64$	0.0175	0.0143	0.0123	0.0123
$n = 81$	0.0164	0.0133	0.0113	0.0112
$n = 100$	0.0151	0.0123	0.0103	0.0103
$n = 121$	0.0142	0.0115	0.0095	0.0095

Table 2: Standard deviation of $\hat{\beta}_1$ values.

$\hat{\sigma}(\hat{\beta}_2)$	Algorithm 1	Algorithm 2	Algorithm 3	Algorithm 4
$n = 4$	0.0087	0.0089	0.0050	0.0054
$n = 9$	0.0080	0.0077	0.0042	0.0048
$n = 16$	0.0066	0.0066	0.0038	0.0044
$n = 25$	0.0059	0.0060	0.0045	0.0045
$n = 36$	0.0054	0.0055	0.0048	0.0048
$n = 49$	0.0053	0.0052	0.0050	0.0050
$n = 64$	0.0048	0.0047	0.0047	0.0046
$n = 81$	0.0045	0.0044	0.0046	0.0046
$n = 100$	0.0041	0.0041	0.0046	0.0048
$n = 121$	0.0038	0.0038	0.0044	0.0045

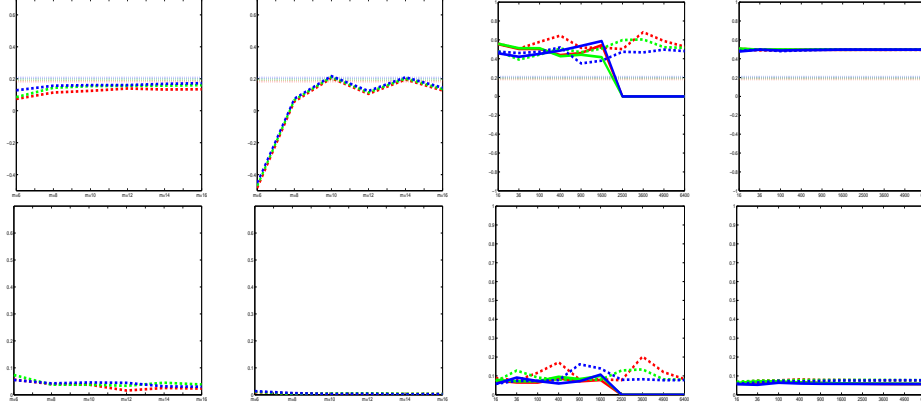Table 3: Standard deviation of $\hat{\beta}_2$ values.

Figure 2: $\hat{\nu}$, $\hat{\beta}_1$, and $\hat{\beta}_2$ values (top) and standard deviations (bottom), partially-integrated method (left), marginal-integrated method (left-medium), algorithm 3 (right-medium), algorithm 4 (right), for case I and for model (9) with $\sigma_{\varepsilon_2} = 2 * 10^2$. The values on horizontal axis represent the spectral curve sample sizes considered.

appreciated in the temporal long-range dependence parameter estimates. After computing the corresponding least-squares plug-in estimators of the values of the original process, it is observed a better performance of the plug-in predictor based on the parameter estimation in the spectral-wavelet domain. Note that the order of magnitude of the absolute error is less than 0.1 with the proposed methodology, while with the previous spectral methods in Frías *et al.* (2006) and Frías *et al.* (2009) is always larger than 0.1. Therefore, we conclude, as in the simulation study, that for strong-dependence parameter values close to Case I, a better performance is obtained with the proposed methodology in the spectral-wavelet domain, in terms of Algorithms 1 and 2.

6. Final comments

Long-range dependence is a key feature in the analysis of complex systems which can be equivalently studied, thanks to Tauberian-type theorems (see, for example, Leonenko (1999)), in terms of the local singularity level, in a neighborhood of the zero frequency, of the spectral density. This fact motivates the parameter estimation methodology proposed in this paper, in terms of compactly supported wavelet functions. The estimation algorithms proposed combine thresholding in the wavelet domain with linear regression from the log-thresholded-wavelet transform of the spectral data. This double filtering is advisable in the cases showed in the simulation study, thus, for processing spectral data displaying high local singularity, due to the heavy tail behavior of the covariance function, and to the local variability of the observation noise. As main conclusion conducted from the paper, we then have that Algorithms 1 and 2 are suitable for processing high local structural spectral variability, corresponding to the range $(0.3, 0.5)$, after applying hard-thresholding in the presence of measurement noise.

On the other hand, the consistency of the wavelet-spectral based estimators formulated for the approximation of the long-range dependence parameters follows from the consistency of the wavelet periodogram, computed from the functional spectral data (see Frías and Ruiz-Medina (2012)). Thus, the efficiency and consistency of these estimators, with a suitable
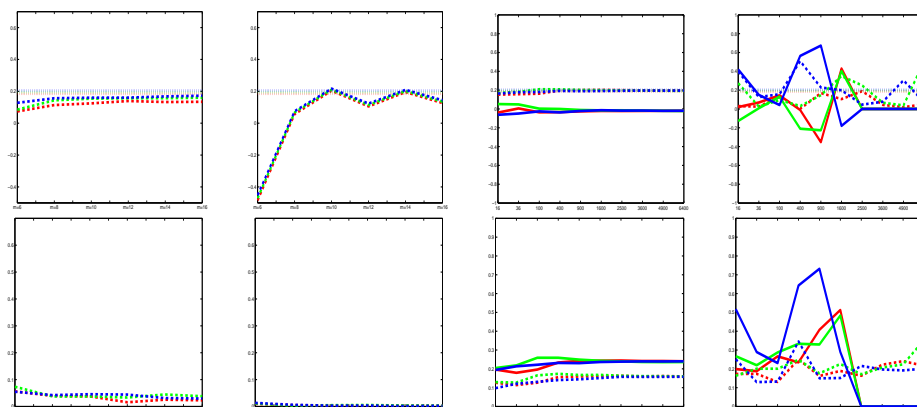
Figure 3: $\hat{\nu}$, $\hat{\beta}_1$, and $\hat{\beta}_2$ values (top) and standard deviations (bottom), partially-integrated method (left), marginal-integrated method (left-medium) algorithm 1 (right-medium), algorithm 2 (right), for case II and for model (9) with $\sigma_{\varepsilon_2} = 2 * 10^2$. The values on horizontal axis represent the spectral curve sample sizes considered.

scaling, ensure a good performance when the functional sample size increases.

References

Adler RJ (1981). *The Geometry of Random Fields.* Wiley, London.

Akkaya AD, Yücemen MS (2002). "Stochastic modeling of earthquake occurrences and estimation of seismic hazard: a random field approach." *Probabilistic Engineering Mechanics*, pp. 1–13.

Anh VV, Lam KC, Leung Y, Tieng Q (2000). "Multifractal analysis of Hong Kong air quality data." *Environmetrics*, pp. 139–149.

Baladandayuthapani V, Mallick B, Hong M, Lupton J, Turner N, Caroll R (2008). "Bayesian hierarchical spatially correlated functional data analysis with application to colon carcinoginesis." *Biometrics*, pp. 64–73.

Bardet JM, Lang G, Oppenheim G, Philippe A, Stove S, Taqqu MS (2003). "Semi-parametric estimation of the long-range dependence parameter." *In: Doukhan P, Oppenheim G, Taqqu M (Eds) Theory and Applications of Long-Range Dependence.*

Basse M, Diop A, Dabo-Niang S (2008). *Mean squares properties of a class of kernel density estimates for spatial functional random variables.* Technical Report, Université Gaston Berger de Saint-Louis, Senegal.

Bell JH, BA BB, Martini (2010). "Imaging spectroscopy of jarosite cement in the Jurassic Navajo Sandstone." *Remote Sensing of Environment*, pp. 2259–2270.
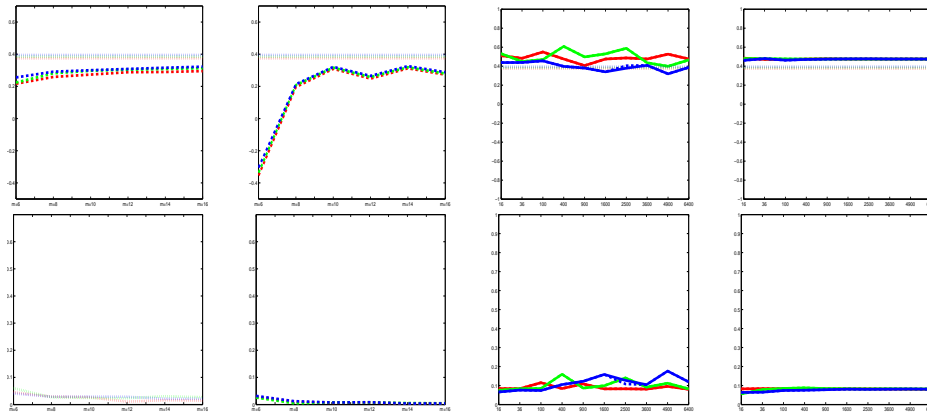
Figure 4: $\hat{\nu}$, $\hat{\beta}_1$, and $\hat{\beta}_2$ values (top) and standard deviations (bottom), partially-integrated method (left), marginal-integrated method (left-medium) algorithm 3 (right-medium), algorithm 4 (right), for case II and for model (9) with $\sigma_{\varepsilon_2} = 2 * 10^2$. The values on horizontal axis represent the spectral curve sample sizes considered.

Benhenni K, Hedli-Griche S, Rachdia M, Vieu P (2008). "Consistency of the regression estimator with functional data under long memory conditions." *Statistics and Probability Letters*, pp. 1043–1049.

Byambakhuu I, Sugita M, Matsushima D (2010). "Spectral unmixing model to assess land cover fractions in Mongolian steppe regions." *Remote Sensing of Environment*, pp. 2361–2372.

Clark RN, Roush TL (1984). "Reflectance Spectroscopy: Quantitative analysis techniques for remote sensing applications." *Journal of Geophysical Research*, pp. 6329–6340.

Delicado P, Giraldo R, Comas C, Mateu J (2009). "Statistics for spatial functional data: some recent contributions." *Environmetrics*, pp. 224–239.

Donoho DL, Johnstone IM (1995). "Adapting to unknown smoothness via wavelet shrinkage." *Journal of the American Statistical Association*, pp. 1200–1224.

Elvidge CD, Chen Z, Groeneveld DP (1993). "Detection of trace quantities of green vegetation in 1990 AVIRIS data." *Remote Sensing of Environment*, pp. 271–279.

Ferraty F, Goia A, Vieu P (2002). "Functional nonparametric model for time series: a fractal approach for dimension reduction." *Test*, pp. 317–344.

Frías MP, Ruiz-Medina MD (2012). "Wavelet-Based Estimation of Anisotropic Spatiotemporal Long-Range Dependence." *Methodology and Computing in Applied Probability (in progress, submitted the revised version)*.

Frías MP, Ruiz-Medina MD, Alonso FJ, Angulo JM (2006). "Semiparametric Estimation of Spatiotemporal Anisotropic Long-Range Dependence." In *Proceedings in Computational Statistics (Contributed Paper)*.

Figure 5: $\hat{\nu}$, $\hat{\beta}_1$, and $\hat{\beta}_2$ values (top) and standard deviations (bottom), partially-integrated method (left), marginal-integrated method (left-medium), algorithm 1 (right-medium), algorithm 2 (right), for case I and for model (10) with $\sigma_{\varepsilon_2} = 2 * 10^2$. The values on horizontal axis represent the spectral curve sample sizes considered.

Frías MP, Ruiz-Medina MD, Alonso FJ, Angulo JM (2006a). "Spatiotemporal Generation of Long-Range Dependence Models and Estimation." _Environmetrics_, **17**, 139–146.

Frías MP, Ruiz-Medina MD, Alonso FJ, Angulo JM (2008). "Parameter Estimation of Self-Similar Spatial Covariogram Models." _Commputation Statatistics - Theory and Methods_, **37**, 1011–1023.

Frías MP, Ruiz-Medina MD, Alonso FJ, Angulo JM (2009). "Spectral-Marginal-Based Estimation of Spatiotemporal Long-Range Dependence." _Commputation Statatistics - Theory and Methods_, **38**, 103–114.

Gallo K, McNab AL, Karl TR, Brown JF, Hood JJ, Tarpley JD (1993). "The use of a vegetation index for assessment of the urban heat island effect." _International Journal of Remote Sensing_, **14,11**, 2223–2230.

Goetz AFH, Vane G, Solomon JE, Rock BN (1985). "Imaging spectrometry for earth remote sensing." _Journal of Time Series Analysis_, **228**, 1147–1153.

Kelbert M, Leonenko N, Ruiz-Medina MD (2005). "Fractional Random Fields Associated with Stochastic Fractional Heat Equation." _Advances in Applied Probability_, **37**, 108–133.

Leonenko N (1999). _Limit Theorems for Random Fields with Singular Spectrum. Mathematics and its Applications_. Kluwer Academic Publishers, Dordrecht, Boston, London.

Marguerit C, Schertzed D, Schmitt F, Lovenjoy S (1998). "Copepod diffusion within multi-fractal phytoplankton fields." _Journal of Marine Systems_, **16**, 69–83.

Meyer Y (1992). _Wavelet and Operators_. Cambridge University Press, Cambridge.

Price JC (1990). "Using spatial context in satellite data to infer regional scale evapotranspiration." _I.E.E.E. Transactions on Geoscience and Remote Sensing_, **28**, 940–948.
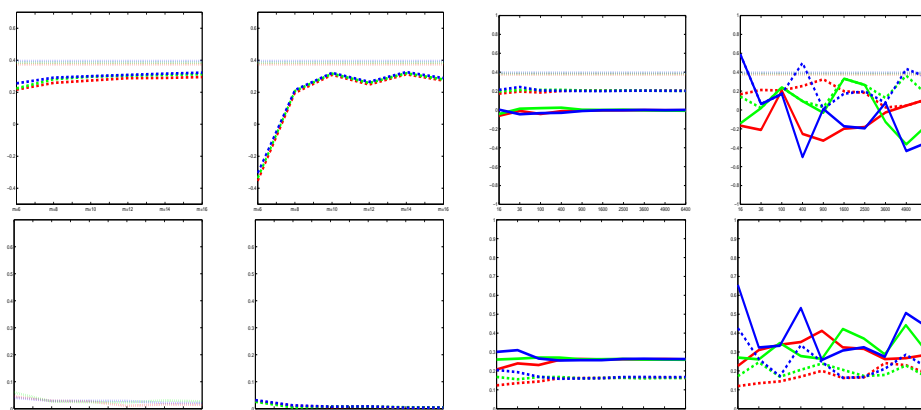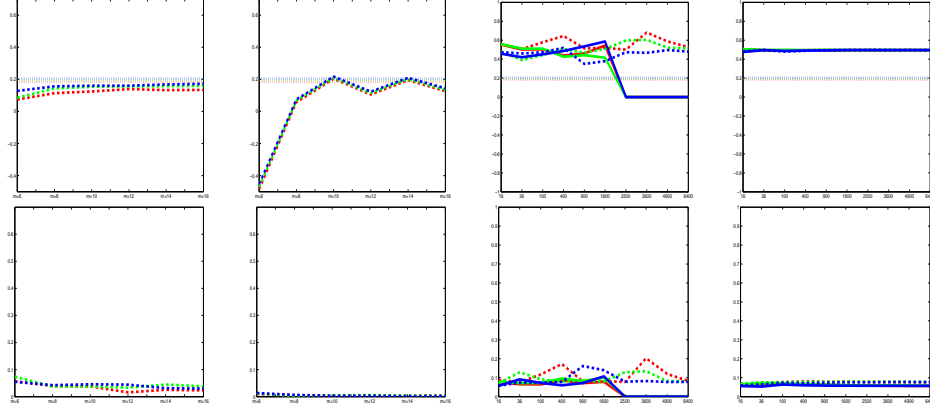
Figure 6: $\hat{\nu}$, $\hat{\beta}_1$, and $\hat{\beta}_2$ values (top) and standard deviations (bottom), partially-integrated method (left), marginal-integrated method (left-medium), algorithm 3 (right-medium), algorithm 4 (right), for case I and for model (10) with $\sigma_{\varepsilon_2} = 2*10^2$. The values on horizontal axis represent the spectral curve sample sizes considered.

Ruiz-Medina MD (2011). "Spatial autoregressive and moving average Hilbertian processes." *Journal of Multivariate Analysis*, **102**, 292–305.

Ruiz-Medina MD, Ángulo JM, Anh V (2003). "Fractional generalized random fields on bounded domains." *Stochastics Analysis and Applications*, **21**, 465–492.

Vidakovic B (1999). *Statistical Modeling by Wavelets*. Wiley Series in Probability and Statistics.

Affiliation:

María Dolores Ruiz-Medina
Faculty of Sciences
University of Granada
Campus Fuente Nueva s/n
18071 Granada , Spain
E-mail: mruiz@ugr.es
URL: http://www.ugr.es/~mruiz

Journal of Environmental Statistics
Volume 3, Issue 2
July 2012

http://www.jenvstat.org
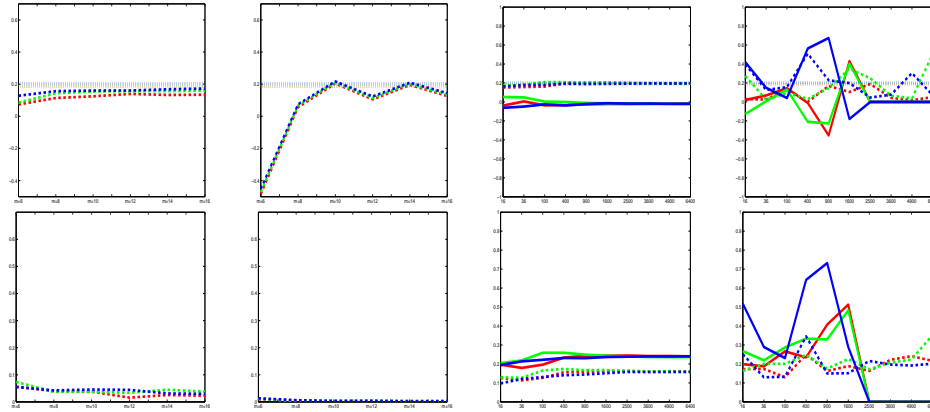Submitted: 2011-05-24
Accepted: 2012-07-09

Figure 7: $\hat{\nu}$, $\hat{\beta}_1$, and $\hat{\beta}_2$ values (top) and standard deviations (bottom) partially-integrated method (left), marginal-integrated method (left-medium), algorithm 1 (right-medium), algorithm 2 (right), for case II and for model (10) with $\sigma_{\varepsilon_2} = 2 * 10^2$. The values on horizontal axis represent the spectral curve sample sizes considered.

Figure 8: $\hat{\nu}$, $\hat{\beta}_1$, and $\hat{\beta}_2$ values (top) and standard deviations (bottom) partially-integrated method (left), marginal-integrated method (left-medium), algorithm 3 (right-medium), algorithm 4 (right), for case II and for model (10) with $\sigma_{\varepsilon_2} = 2 * 10^2$. The values on horizontal axis represent the spectral curve sample sizes considered.
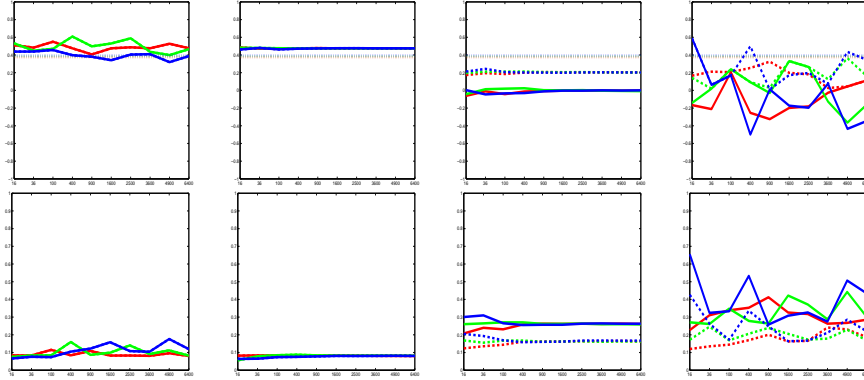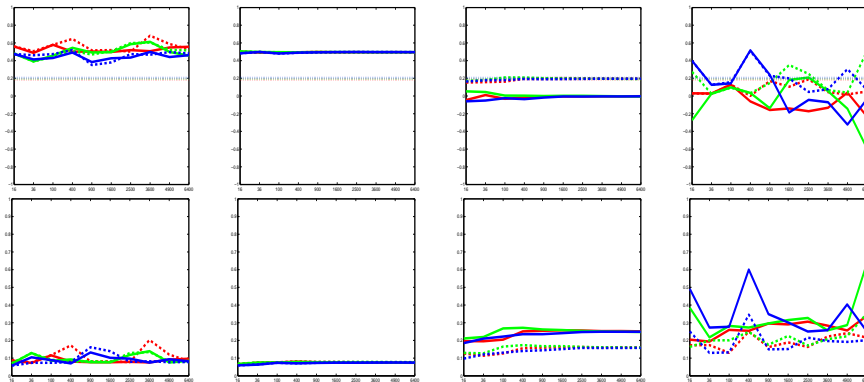
Figure 9: $\hat{\nu}$, $\hat{\beta}_1$, and $\hat{\beta}_2$ values (top) and standard deviations (bottom), algorithm 1 (left), algorithm 2 (left-medium,), algorithm 3 (right-medium), algorithm 4 (right), for case I and for model (10) with $\sigma_{\varepsilon_2} = 0.05 * 10^2$. The values on horizontal axis represent the spectral curve sample sizes considered.

Figure 10: $\hat{\nu}$, $\hat{\beta}_1$, and $\hat{\beta}_2$ values (top) and standard deviations (bottom) algorithm 1 (left), algorithm 2 (left-medium,), algorithm 3 (right-medium), algorithm 4 (right), for case II and for model (9) with $\sigma_{\varepsilon_2} = 0.05 * 10^2$. The values on horizontal axis represent the spectral curve sample sizes considered.
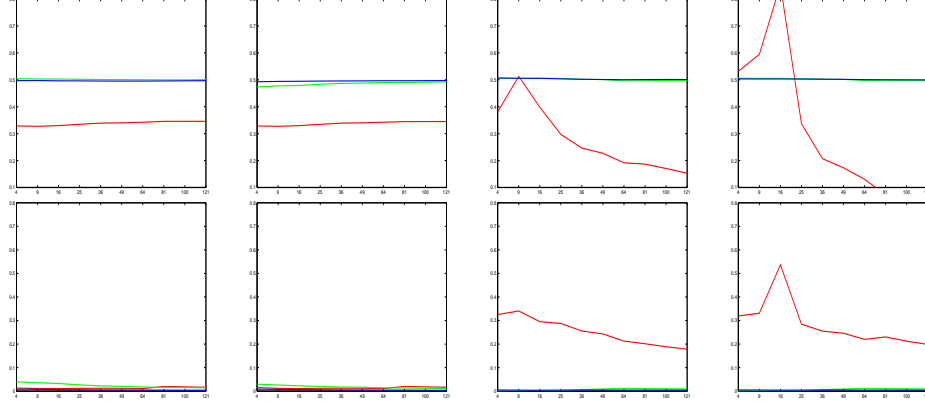
Figure 11: $\hat{\nu}$ (red), $\hat{\beta}_1$, (green) and $\hat{\beta}_2$ (blue) values (top) and standard deviations (bottom), algorithm 1 (left), algorithm 2 (left-medium), algorithm 3 (right-medium), algorithm 4 (right). The values on horizontal axis represent the spectral curve sample sizes considered.
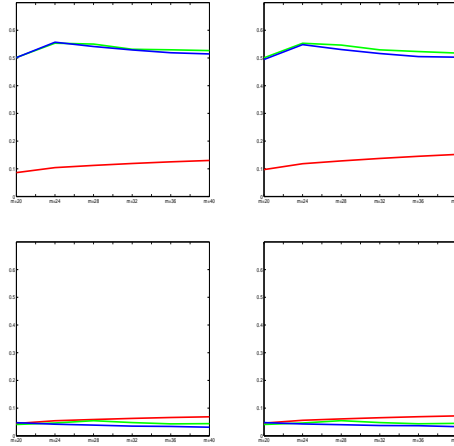

Figure 12: $\hat{\nu}$ (red), $\hat{\beta}_1$ (green) and $\hat{\beta}_2$ (blue) values (top) and standard deviations method (left), marginal-integrated method (right).